NANO LETTERS

Letter

pubs.acs.org/NanoLett

Measuring Spatially Resolved Collective Ionic Transport on Lithium Battery Cathodes Using Atomic Force Microscopy

Aaron Mascaro,*[,†] Zi Wang,[‡] Pierre Hovington,[¶] Yoichi Miyahara,[†] Andrea Paolella,[¶] Vincent Gariepy,[¶] Zimin Feng,[¶] Tyler Enright,[†] Connor Aiken,[†] Karim Zaghib,[¶] Kirk H. Bevan,[‡] and Peter Grutter[†]

[†]Department of Physics, McGill University, 3600 rue University, Montreal, Québec H3A2T8, Canada

[‡]Materials Engineering, McGill University, 3610 rue University, Montreal, Québec H3A0C5, Canada

[¶]Institut de Recherche d'Hydro Québec, 1800 Boulevard Lionel-Boulet, Varennes, Québec J3X1S1, Canada

S *Supporting Information*

ABSTRACT: One of the main challenges in improving fast charging lithium-ion batteries is the development of suitable active materials for cathodes and anodes. Many materials suffer from unacceptable structural changes under high currents and/or low intrinsic conductivities. Experimental measurements are required to optimize these properties, but few techniques are able to spatially resolve ionic transport properties at small length scales. Here we demonstrate an atomic force microscope (AFM)-based technique to measure local ionic transport on $LiFePO_4$ to correlate with the structural and compositional analysis of the same region. By comparing the measured values with density functional theory (DFT) calculations, we demonstrate that Coulomb interactions between ions give rise to a collective activation energy for ionic transport that is dominated by large phase boundary hopping barriers. We successfully measure both the collective activation energy and the smaller single-ion bulk hopping barrier and obtain excellent agreement with values obtained from our DFT calculations.

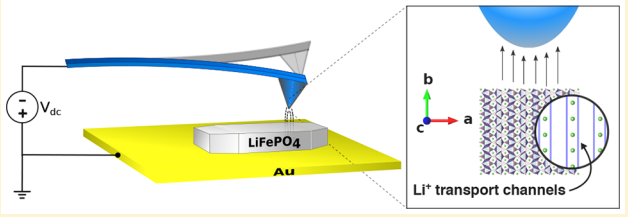

KEYWORDS: *Lithium ion battery, atomic force microscopy, ionic transport, lithium iron phosphate*

A major challenge in the widespread deployment of sustainable energy sources such as solar and wind is maintaining grid stability due to their time varying nature. Distributed energy storage in electric vehicle batteries is an attractive option to stabilize the grid. Since private vehicles are only used for 1 h per day on average,[1] batteries in electric vehicles could be connected to the grid for the remaining 23 h per day. Power utilities could then develop the infrastructure to both charge and discharge the batteries as needed in order to stabilize the grid. A major issue inhibiting widespread consumer acceptance and thus broader deployment of this concept is the low maximum charge rate (c-rate) of the current battery materials and chemistries. The maximum c-rate for most lithium-ion batteries is typically limited by low electronic and ionic conductivity in the cathode or unacceptable structural changes under high charging currents.[2,3] In order to improve these transport properties, a fundamental understanding of their underlying mechanisms is essential, but lacking. Measurements of many properties such as activation energy for ionic transport, in particular, differ significantly from values obtained from modeling. Here we show through both experiment and theory that for ionic transport through solids this discrepancy arises due to the collective transport behavior of the ions.

It is generally accepted that lithium transport primarily takes place along 1-dimensional channels oriented along the [010] axis in $LiFePO_4$ (see Figure 1A), while cross-channel diffusion is possible by a concerted process involving two lithium ions along the [001] axis; the channels are effectively blocked along the [100] axis making transport impossible in this direction. This was first predicted by calculating the hopping barriers for several possible migration paths and then demonstrated by high-temperature neutron diffraction experiments.[4,5] Most calculations of the minimum lithium hopping barrier (i.e., along the [010] direction) found values in the range of ~0.3 eV,[6−10] which is significantly smaller than many experimentally measured values (~0.5 eV).[4,11−15] These calculations typically involve a single lithium ion hopping through an $FePO_4$ lattice and do not take into account the effects of differing polaronic environments as well as neighboring ions. As we will show, these calculations are extremely sensitive to the surrounding polarons and ions. Their results must also be compared with techniques that measure equivalent phenomena, namely, bulk ionic hopping barriers, which we have done using electrostatic force microscopy (EFM) in the time-domain.

The first measurement of ionic conductivity using AFM was demonstrated by Bennewitz and co-workers where the conductivity of F^- ions in CaF_2 was probed by measuring the relaxation as a function of time after applying a step potential.[16]

Received: May 3, 2017
Revised: June 14, 2017
Published: June 19, 2017

ACS Publications © 2017 American Chemical Society

DOI: 10.1021/acs.nanolett.7b01857
Nano Lett. 2017, 17, 4489−4496

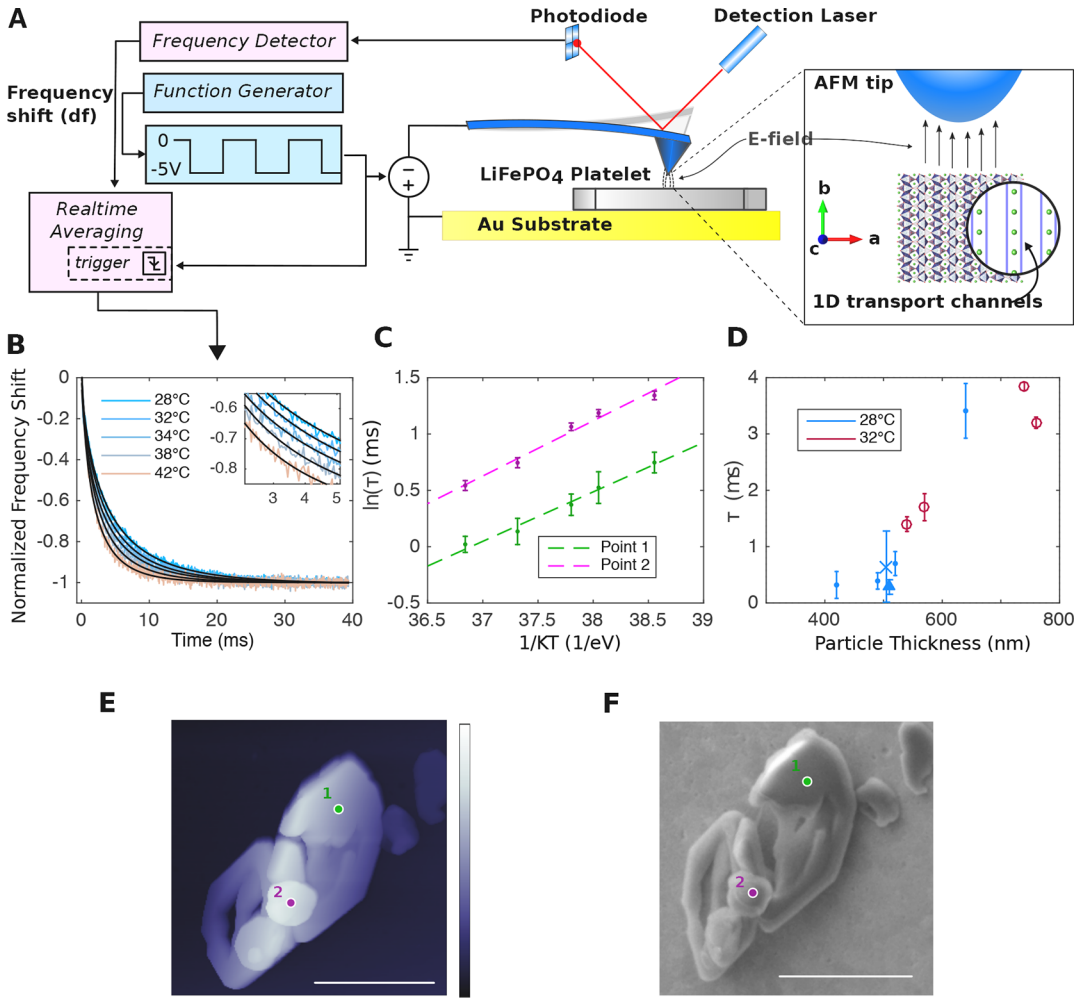

Figure 1. Localized time-domain spectroscopy of ionic transport on pure $LiFePO_4$ platelets using AFM. (A) Block diagram of AFM electrostatic force spectroscopy measurement. Inset illustrates crystallographic direction with closeup of 1D transport channels of $LiFePO_4$ platelet with respect to the applied electric field between the AFM tip and back electrode (gold substrate). (B) Example of averaged frequency shift vs time curves (normalized for clarity) obtained after realtime averaging of 100 pulses for slower responses (<34 °C) and 700 pulses for faster responses. Black lines are fits obtained using eq 2; inset shows a close-up of the data and fitted curves from 2 to 5 ms. (C) Arrhenius plot of the natural log of the time constants (in ms) obtained from fitted decay curves vs $1/kT$ and their best-fit lines for both points labeled in (E). Error bars represent the standard deviation of time constants obtained at each point for each temperature (see Methods). (D) Time constant obtained by fitting frequency shift vs time curves taken at various points on four different particles (indicated by different symbols) plotted against the particle thickness. (E) Tapping mode topography AFM image of pure $LiFePO_4$ platelets on gold substrate with probe points labeled. (F) SEM image of the same platelets taken while conducting EBSD measurements. All scale bars are 2 μm.

More recent developments in AFM-based techniques have aimed to exploit the high spatial resolution afforded by the nanometer-sized AFM tip to correlate local ionic transport with topography. These include nanoimpedance spectroscopy;[17] electrochemical strain microscopy (ESM),[18,19] which measures the strain response to applied bias pulses; and time-domain electrostatic force microscopy,[20] which measures the relaxation as a function of time similar to the measurement performed by Bennewitz et al.[16] The technique we have employed is an extension of the time-domain method to faster time scales using fast detection electronics and ultrahigh frequency AFM cantilevers (see Methods).

Ionic transport in solids is a vacancy-mediated process involving discrete hops by ions in a lattice from their initial sites to neighboring vacant sites. Applying an electric field to an ionic conductor causes the ions to move in response to the field applied through the material. Ionic hopping leads to, and can thus be observed as, a decay of the internal electric field, $\phi(t)$. On very short time scales (shorter than some cutoff time t_c, $t_c \approx$ ps according to ref 21), the decay is accurately described by a simple exponential as in eq 1. However, on longer time scales the electric field decays as a stretched exponential as in eq 2:[21,22]

$$\phi(t) = \exp[-t/\tau] \quad \text{for } t < t_c \tag{1}$$

$$\phi(t) = \exp[-(t/\tau^*)^{\beta}] \quad \text{for } t > t_c,\ 0 < \beta < 1 \tag{2}$$

where β is the stretching factor, τ is the time constant for individual ionic hops at short time scales, and τ^* is the effective time constant that is observed over time scales larger than t_c. This transition is due to the fact that beyond the cutoff time, ionic hopping is no longer random because the probability of a specific hop occurring is influenced by the previous hops of nearby ions. This process was described by the "coupling model" by Ngai,[23] and this result (eqs 1 and 2) also appears in the "jump relaxation model" by Funke.[22] These models are

DOI: 10.1021/acs.nanolett.7b01857
Nano Lett. 2017, 17, 4489−4496

both very similar in many ways and even though their approaches are quite different, they obtain the same result in the time regime of interest for this application.[22]

The relaxation time constant (τ^*) varies with temperature according to the Arrhenius law:

$$\tau^* = \tau_\infty^* \exp(E_a^*/kT) \quad (3)$$

where E_a^* is the effective activation energy (for collective transport), τ_∞^* is the effective attempt rate, k the Boltzmann constant, and T temperature. Ngai and co-workers showed that E_a^* is not the energy barrier encountered by individual ions, but rather an overall activation energy for collective ionic transport through a material (i.e., the effective activation energy).[21,23] This is due to the Coulomb interactions between ions, which cause the local energy landscape to change as neighboring ions hop into vacant sites. An intuitive description of this process is as follows: an ion that has hopped into a higher energy site can either hop back into its original site to lower the energy, or the surrounding ions can reorganize around it in a correlated relaxation effect. If a backward hop by the initial ion requires less energy than the neighboring ions relaxing around it, it has a higher probability of occurring. However, on long enough time-scales ($\gg t_c$), the neighboring ions reorganize to sufficiently raise the backward hopping barrier so that the less-likely forward hopping event does occur; this gives rise to net transport and effectively dominates any signal related to charge transport in these systems.[22,24] The single-ion hopping barrier (for hopping through the bulk phase), E_a, can be recovered by the following relation:

$$E_a = \beta E_a^* \quad (4)$$

Since E_a is the single-ion bulk-phase hopping barrier, it can therefore be directly compared with the theoretical energy barrier obtained from modeling. The collective transport activation energy E_a^*, however, is the quantity typically measured using conventional techniques such as impedance spectroscopy. E_a can be recovered from impedance spectroscopy measurements by power law analysis with $\sigma(\omega) \propto (\omega\tau)^n$ where $\beta = 1 - n$ in the intermediate (dispersive) frequency regime, although this analysis is seldom done.[22,23,25,26]

The time-domain electrostatic force spectroscopy technique was originally developed by Schirmeisen et al.[20] where a step potential is applied between a conductive AFM tip and sample and the measured interaction (i.e., change in cantilever resonance frequency) is recorded over time. This technique has been successfully used to measure Li^+ transport in $LiAlSiO_4$ with varying degrees of crystallinity, K^+ transport in $K_2O{\cdot}2CaO{\cdot}4SiO_2$ (KCS) glass, and Na^+ transport in $Na_2O{\cdot}GeO_2$ (NG) glass samples.[20,27−29] The electric field generated inside the bulk is perpendicular to the surface in the region directly under the tip (Figure 1A), which causes ions to move as they attempt to shield the internal field. As charge builds up on the surface directly beneath the AFM tip, the electric field at the tip increases. An increased electric field leads to a stronger attractive tip−sample force, which manifests as a reduction in cantilever resonance frequency. Recording the resonance frequency over time gives the ionic response signal directly that can be fitted to the general form of the ionic response, eq 2. The ionic conductors probed previously all had relaxation times on the order of seconds and could thus be measured using AFM detection techniques under normal operating conditions. $LiFePO_4$, however, has relaxation times on the order of milliseconds at room temperature, thus requiring high-speed frequency detection electronics and an averaging protocol to reduce noise, which we have developed and implemented (see Methods).

$LiFePO_4$ is a well-characterized and relevant material for high power-density batteries and is a good candidate for furthering our understanding of ionic transport in solids. A hydrothermally synthesized $LiFePO_4$ platelet (see Methods) on a gold substrate was probed using the high-speed electrostatic force spectroscopy technique with a step potential of −5 V applied to the tip at five different temperatures. The frequency shift values were recorded over 40 ms and averaged 100 to 700 times to obtain an acceptable signal-to-noise ratio (SNR). The measurements were performed at a tip−sample separation of ∼20 nm. Altering the lift height showed no change on the measured relaxation times, the only change was the absolute value of the saturation frequency shift, which is one of the fit parameters. A block diagram of the probe measurements is shown in Figure 1A, while the resulting frequency shift vs time traces are shown in Figure 1B (see Methods).

The two points probed on this particle are indicated in the tapping-mode AFM topography image (see Methods) in Figure 1E. Hydrothermally synthesized $LiFePO_4$ platelets are known to form with the largest facet in the *ac*-plane, meaning that the [010] axis in these particles is perpendicular to the surface being probed.[30] This was verified using electron backscatter diffraction (EBSD, see Figure S1). The scanning electron microscope (SEM) image taken simultaneously is shown in Figure 1F. Thus, the 1D transport channels along the [010] axis are oriented directly along the applied electric field from the AFM tip, illustrated in the inset of Figure 1A. The Arrhenius plot of the relaxation time constants τ^* is shown in Figure 1C along with linear fits to the natural log of the relaxation time vs $1/kT$, which give us the effective attempt rate, τ_∞^*, and the activation energy for collective ionic transport, E_a^*, as per eq 3. The collective ionic transport activation energy (0.47 eV) is very similar to values reported from several other techniques for transport along the [010] direction.[4,11−15] Using eq 4 we see that the single-ion energy barrier for bulk hopping is around 0.3 eV, which is in very good agreement with values reported from modeling.[4] The results are summarized in Table 1 (see Table S1 for full fitting results).

Table 1. Summary of the Results Obtained for Transport along the [010] Direction from Points 1 and 2 in Figure 1E[a]

	theory	experiment
collective activation energy (eV)	0.5−0.6	0.47(7)
bulk hopping barrier (eV)	0.31−0.33	0.30(4)
collective diffusivity (cm^2/s)	2×10^{-13}	$2.8(4) \times 10^{-13}$
bulk diffusivity (cm^2/s)	1×10^{-9}	$0.2 \pm 2.0 \times 10^{-10}$

[a]Theoretical diffusivity values were obtained using eq 5 with a ν^* value of $2 \times 10^{12} s^{-1}$. T = 300 K was used for all diffusivity calculations. Uncertainties are the standard deviation values obtained from the parametric bootstrap analysis (see Methods).

After probing several particles with varying thicknesses we observed a clear trend of increasing relaxation time with increasing particle thickness (Figure 1D). This indicates that the ionic transport being probed is truly a bulk effect that involves the collective motion of all the ions in the channels in this high lithium-ion concentration limit (i.e., low-vacancy concentration). The electronic conductivity of $LiFePO_4$ is

DOI: 10.1021/acs.nanolett.7b01857
Nano Lett. 2017, 17, 4489−4496

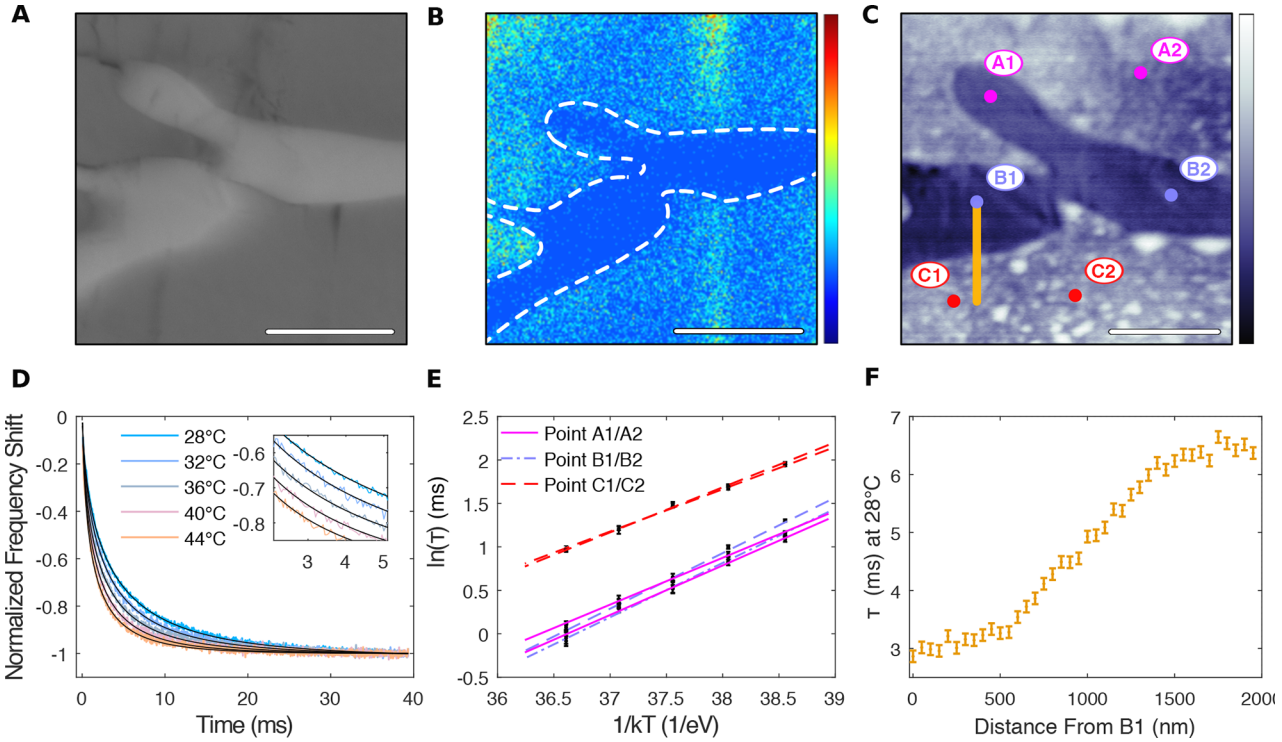

Figure 2. Composition and ionic transport on bulk partially delithiated $LiFePO_4$. (A) SEM secondary electron image of the region of interest. (B) TOF-SIMS map of Li_7^+ counts with the grain boundaries outlined (white dashed lines); the color scale indicates Li_7^+ counts/TOF-SIMS extraction from 0 to 0.08, the center region is clearly lithium-poor, while the upper and lower regions are lithium-rich. (C) FM-AFM topography, vertical scale extends from 0 (black) to 35 nm (white). Each labeled point was probed using the electrostatic force spectroscopy technique (see text). (D) Example of frequency shift (normalized for clarity) vs time data for five temperature values taken at point A2 in (C). Black lines are fits obtained using eq 2; inset shows a close-up of the data and fitted curves from 2 to 5 ms. (E) Arrhenius plot of the natural log of the relaxation times (in ms) obtained from fitted decay curves vs $1/kT$ and their best-fit lines (solid, dash-dot, and dashed lines) for all points labeled in (C). Error bars represent the standard deviation of relaxation times obtained at each point for each temperature (see Methods). (F) Spatial variation of relaxation time (τ) taken along line indicated in (C) with 50 nm spacing between points, error bars are the standard deviations of the measurements done at points B1 and C1 (100 μs). All scale bars are 2 μm.

several orders of magnitude higher than the ionic conductivity;[13] thus, the electronic polarization takes place much faster than the ionic transport probed here. The result is a relaxation signal due entirely to the Li^+ transport. Measurements were also done on both conducting and insulating samples without mobile ions present, and no response was observed, demonstrating that ionic transport is truly the origin of the observed signal (see Figure S2). To further investigate the observed relaxation, probe experiments were also conducted with −4 and −5 V applied on the same location (see Figure S3). The time constant and stretching factors obtained after fitting were identical. The only notable effect is a difference in the maximum frequency shift value due to the quadratic dependence of frequency shift on applied voltage (see Methods).

A partially delithiated Li_xFePO_4 ingot with large grain sizes was synthesized and characterized using various techniques to correlate local structure with local ionic transport properties (see Methods). X-ray diffraction was used to check the bulk phase purity. $LiFePO_4$ and $FePO_4$ phases were identified in ~80:20 wt % ratio, and only trace amounts of $K_2S_2O_8$ were found. Figure 2A shows a scanning electron microscope (SEM) secondary-electron image of the sample. The local composition of this exact region of the sample was further investigated using time-of-flight secondary ion mass spectrometry (TOF-SIMS, see Methods). The TOF-SIMS mapping of Li_7^+ is shown in Figure 2B with an outline of the center region (light region in the SEM image) drawn to guide the eye. Figure 2C shows the frequency-modulated AFM (FM-AFM) topography image taken over the same region of interest. The TOF-SIMS mapping clearly shows that region B (also containing point A1 as indicated in the topography image) is lithium-poor, while the outer regions (C and A2) are lithium-rich. It has been shown that chemically delithiated Li_xFePO_4 spontaneously phase segregates into lithium-rich ($x \approx 1$) and lithium-poor ($x \approx 0$) regions;[31] thus, the upper and lower regions in the TOF-SIMS data are nearly fully lithiated ($x \approx 1$), while the center region is nearly fully delithiated ($x \approx 0$).

Each point labeled in Figure 2C was probed using the high-speed electrostatic force spectroscopy technique. A summary of the activation energies and bulk hopping barriers measured in each of the three regions (A,B,C) is shown in Table 2. The full results including stretching factors, and attempt frequencies for all six points are found in Table S2. With the exception of region B, the activation energies and hopping barriers are identical to those measured on the platelet sample. The slightly higher collective activation energy and hopping barrier in region B is most likely due to an increased concentration of antisite defects resulting from the delithiation process. This has been shown to force ions to follow a 2D transport pathway along the (010) and (001) directions with a higher hopping barrier of ~0.36 eV, which is consistent with our measured values.[32,33] This region still displays the collective transport

DOI: 10.1021/acs.nanolett.7b01857
Nano Lett. 2017, 17, 4489−4496

Table 2. Summary of the Results Obtained for the Three Regions Labeled in Figure 2C[a]

	A	B	C
collective activation energy (eV)	0.54(3)	0.62(4)	0.50(1)
bulk hopping barrier (eV)	0.30(1)	0.37(1)	0.32(1)
collective diffusivity (cm^2/s)	$2.3(1) \times 10^{-13}$	$2.2(1) \times 10^{-13}$	$1.08(3) \times 10^{-13}$
bulk Diffusivity (cm^2/s)	$2(2) \times 10^{-9}$	$3(6) \times 10^{-9}$	$1.1(8) \times 10^{-9}$

[a]Average values for each region (i.e., A1/A2, B1/B2, C1/C2) are reported (see Table S2 for full results). Uncertainties are the standard deviation values obtained from the parametric bootstrap analysis (see Methods).

phenomenon, however, with a collective activation energy significantly higher than the bulk hopping-barrier.

A large variation in relaxation times was also observed between regions B and C, which proved useful for demonstrating spatially resolved measurements as shown in Figure 2F. This variation is most likely due to elastic coherency strain arising from large concentration gradients (due to phase separation during crystallization), which has been shown to significantly affect local chemical potential and collective ionic diffusivity.[34,35] The full transition from the characteristic relaxation time of the center grain to that of the outer grain occurs over ~1 μm. This ~1 μm variation across this boundary is also observed in the Kelvin probe force microscopy (KPFM) image (see Figure S3), indicating that the long length-scale variation is intrinsic to the sample and not the resolution limit

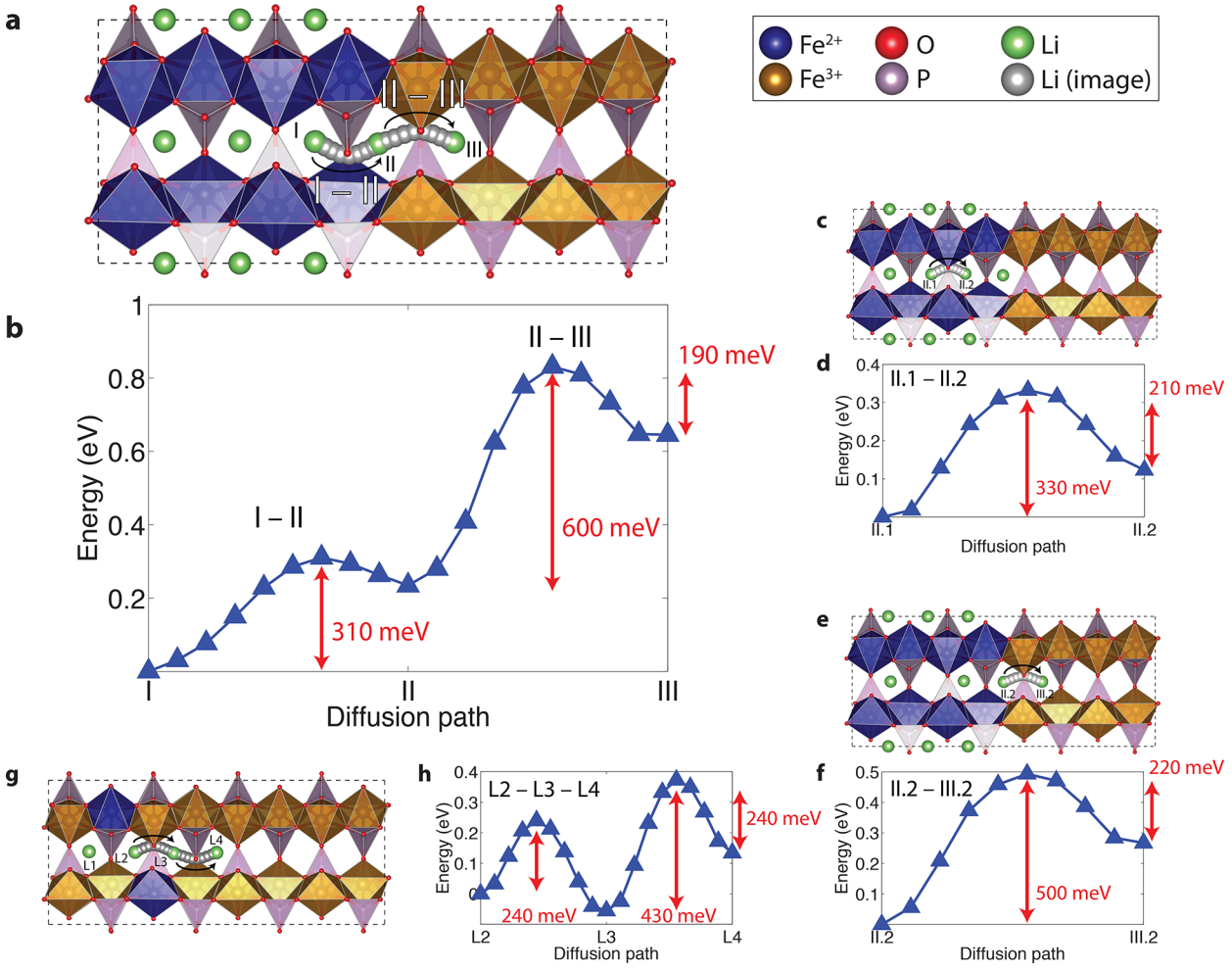

Figure 3. A 1 × 4 × 2 slab of $LiFePO_4$ used for the DFT calculations. Lithium ions are colored in green, oxygen atoms in red, Fe^{2+} (and its O_6 octahedral coordination shell) in blue, and $Fe^{3+}O_6$ in orange. In this 1 × 4 × 2 slab, there is a total of eight layers of sites that can be occupied by Li ions (and a corresponding eight layers of Fe atoms that can take extra electrons from the Li atoms). To simulate a phase boundary, we added three layers of Li ions and four layers of Fe^{2+} on one-half of the slab, with an additional layer of Fe^{2+} added to preserve *b*-axis directional symmetry, while the other half of the slab remains in $FePO_4$ configuration. Intermediate images of the position of the Li ion during hopping are shown in silver. (A) Calculated pathways of the middle rightmost ion hopping from the initial configuration (labeled as I) through the last Fe^{2+} layer to the next site (labeled as II), and further through the $LiFePO_4/FePO_4$ phase boundary to an empty $FePO_4$ site (labeled as III). (B) Calculated energies of the I–II and II–III hopping pathways. (C,D) Calculated pathway and energies of the second Li ion hopping after the first ion has hopped from I to II. The end points of this pathway are labeled as II.1 and II.2. (E,F) Calculated pathway and energies of the first Li ion hopping from the arrangement in (B) and (D) through the phase boundary (II.2 to III.2). (G,H) Calculated pathway and energies in the dilute limit, a configuration with just two Li ions. The first ion is kept at the point labeled as L1, and the second ion is moved from L2 to L3 and finally to L4. The induced polarons are kept at their Fe centers as shown in (G) throughout the calculation. (A), (C), (E), and (G) were produced using VESTA 3.[36]

DOI: 10.1021/acs.nanolett.7b01857
Nano Lett. 2017, 17, 4489–4496

of the technique, which has previously been reported as <100 nm.[27]

EBSD was also conducted on this region and revealed that the $LiFePO_4$ outer regions are not perfectly oriented with the *b*-axis normal to the surface, but still with a component in that direction (see Figure S5). This demonstrates that 1D transport can be probed at least in all but the most extreme cases where the 1D channels have no component along the applied field direction. There was some uncertainty in determining the orientation of the $FePO_4$ center region from the EBSD data, and so it is not reported here (see Supporting Information).

The local diffusivity was calculated using eq 5, where ν^* is the attempt frequency ($1/\tau^*$) and a is the intersite distance (3.07 Å).[4]

$$D = a^2\nu^* \exp(-E_a/kT) \quad (5)$$

Using the collective transport activation energies (E_a^*) to calculate the collective diffusivity, we obtain the same values as reported from other experimental techniques ($\approx 10^{-13}$–10^{-15} cm^2/s).[37−40] However, inputting the experimentally determined single-ion bulk hopping barriers and attempt frequencies, the diffusivity values ($1–3 \times 10^{-9}$ cm^2/s from the ingot sample measurements, $0.2 \pm 2.0 \times 10^{-10}$ cm^2/s from the platelet measurements) are much closer to those calculated from DFT calculations ($\sim 10^{-9}$ cm^2/s, described below).

We performed DFT + U calculations on a $LiFePO_4$ slab ($1 \times 4 \times 2$ unit cells) with carefully controlled polaronic and ionic configurations (see Methods). This is illustrated in Figure 3 where the system is initialized in a partially lithiated state with part of the periodic unit cell in the $LiFePO_4$ phase and the other part in the $FePO_4$ phase. The $LiFePO_4$ phase is a phase segregated cluster containing Li ions and electrons that reduce the surrounding Fe atoms to a 2+ oxidation state. For collective ionic transport to take place, the leading lithium ion must first hop into the nearest vacant site as in Figure 3A. The barrier of the initial hop is highly dependent on the neighboring polaronic structure (Figure 3A,B): if the first hop is within the $LiFePO_4$ phase (i.e., the neighboring Fe atoms are in the 2+ state) the barrier is 0.31 eV, whereas if the first hop is across the $LiFePO_4/FePO_4$ phase boundary the barrier is much larger, either 0.6 or 0.5 eV depending on whether there is a neighboring ion or not (Figure 3C–F). Once the initial hop takes place, the initial ion can either hop back into its original site over a small energy barrier (~0.2 eV) or the next ion can hop into the now vacant site over an energy barrier of 0.33 eV, which is the bulk diffusion barrier. The lower energy event has a much higher probability of occurring, but does not result in net ionic transport. Over a long enough time period the second process will eventually occur. Once the secondary relaxation takes place the remaining ions can hop along the channel over the lower bulk hopping barriers, which are the values reported from previous calculations of ionic hopping barriers (~0.3 eV).[7] This highlights the sensitivity of hopping barriers to their local environment, which must be accounted for in modeling.

To further elucidate this phenomenon, we have studied a configuration in which there are only two Li ions in the same supercell (Figure 3G,H). In this extreme dilute limit there is no phase boundary, although the Li ions and their polarons will prefer a configuration that minimizes their electrostatic interaction energy. Our calculations indicate that the "L3" configuration as shown in Figure 3G is the lowest in energy. The "L2" configuration has a slightly higher total energy, whereas the "L4" configuration is significantly higher in energy. In a fashion analogous to the configurations previously studied, the "L2–L3" barrier is bulk-like, whereas the "L3–L4" barrier is significantly higher. In this configuration, we argue that the higher (and asymmetric) barrier arises mostly due to the Coulomb interactions between the two ions (and their polarons).

Realistically, there are countless different configurations in partially lithiated $LiFePO_4$ and the configurations studied in this work are but a select few of them. The statistical variance can only be revealed by performing an unfeasibly large number of calculations. The studied configurations are, however, self-consistent and both demonstrate the two distinct energy regimes that arise from correlated interactions between multiple lithium ions and their associated polarons. These two regimes (bulk-like diffusion and boundary-crossing events) are present in both ends of the concentration spectrum: high-concentration with phase segregated configurations and the dilute, two-ion limit.

The true meaning of the measured (collective) activation energy and hopping barriers is now more apparent. The E_a^* is the overall activation energy for collective ionic transport, which is dominated (due to the collective motion of ions) by the large local in-channel phase-boundary hopping barriers, whereas the hopping barrier E_a is the energy barrier for a single-ion hopping through the bulk phase. Recall that it is more likely for a leading ion to hop back into its original site over a small energy barrier (~0.2 eV) after completing a phase-boundary hop (II–III in Figure 3A) than for a second ion to hop into the now vacant site over the larger bulk diffusion barrier (~0.3 eV, similar to II.1–II.2 in Figure 3C), but only the latter contributes to net ionic transport. This difference in relative probabilities gives rise to a correlated forward–backward hopping process, leading to dispersive transport governed by eq 2 consistent with our experimental observations. This is supported by the jump relaxation model developed by Funke[22] as well as the dispersive transport picture described by Scher and co-workers.[24]

Recent measurements have shown that a solid solution phase forms during the nonequilibrium stage that occurs during fast charge/discharge.[41,42] Our study indicates that when there is no net external field present, the partially lithiated system will favor phase segregation and clustering on the nanoscale along the 1D transport channels with high initial energetic barriers due to the local phase boundaries. When a strong external field is applied during the measurements (as in charge/discharge) the dispersive behavior of the Li ions will lead to a metastable state where the ionic distribution is such that a solid solution of $LiFePO_4/FePO_4$ forms. Therefore, we have shown that the initial two-phase state and its corresponding high initial hopping barrier lead to the measured collective activation energies, while the hopping barriers in the solid solution state are the bulk hopping barriers and thus lead to the observed fast charge/discharge rates.

We have demonstrated an AFM-based electrostatic force spectroscopy technique to probe local ionic transport properties with high spatial resolution on a $LiFePO_4$ sample. We have successfully correlated these measurements with the local composition and crystallographic structure using SEM, EBSD, and TOF-SIMS. The measured activation energies for collective ionic transport along the [010] direction were in good agreement with typical values obtained using other techniques (~0.5 eV).[4,11−15] Our DFT calculations show that a higher hopping barrier is present as lithium ions cross the $LiFePO_4/$

DOI: 10.1021/acs.nanolett.7b01857
Nano Lett. 2017, 17, 4489–4496

$FePO_4$ phase boundary along the [010] direction (0.5−0.6 eV), which we have identified as the origin of the collective transport activation energy. Moreover, our DFT calculations indicate that the hopping barrier for single-ion transport through the bulk $LiFePO_4$ phase along the [010] direction is ∼0.3 eV, which has also been reported in the literature.[6−9] Through several orders of magnitude improvement in time-resolved AFM measurements, we have demonstrated the ability to extract these single-ion bulk hopping barriers from collective ion motion and obtained values in excellent agreement with both collective ion and single-ion calculations. In conclusion, our AFM-based technique allows for direct correlation of transport properties with the local structure measured using other techniques. By combining these techniques we have refined our understanding of ionic transport to better engineer active materials for high c-rate and high-power lithium-ion batteries. These materials will play a crucial role in the widespread deployment of renewable energy generation and fully electric vehicles with fast charge and discharge requirements.

■ ASSOCIATED CONTENT

Supporting Information

The Supporting Information is available free of charge on the ACS Publications website at DOI: 10.1021/acs.nanolett.7b01857.

Experimental methods; materials preparation; EBSD data; ionic response validation measurements; ionic response at differing applied voltages; KPFM data; KPFM energy level diagrams; ingot sample EBSD data; TOF-SIMS data; $LiFePO_4$ platelet probe data; ingot sample probe data (PDF)

■ AUTHOR INFORMATION

Corresponding Author

*E-mail: mascaroa@physics.mcgill.ca.

ORCID

Aaron Mascaro: 0000-0003-2402-8115

Notes

The authors declare no competing financial interest.

■ ACKNOWLEDGMENTS

The authors acknowledge financial support from the Natural Sciences and Engineering Research Council of Canada and computational support from Canada Foundation for Innovation, Compute Canada, and Calcul Quebec. Z.W. acknowledges financial support from Mitacs of Canada and Fonds Québécois de la Recherche sur la Nature et les Technologies. A.M. would like to acknowledge technical support from Percy Zahl (Brookhaven National Laboratory) in customizing the GXSM software to perform the AFM spectroscopy measurements.

■ REFERENCES

(1) Santos, A.; McGuckin, N.; Nakamoto, H. Y.; Gray, D.; Liss, S. Summary of travel trends: 2009 national household travel survey. http://nhts.ornl.gov/2009/pub/stt.pdf.

(2) Kang, B.; Ceder, G. *Nature* **2009**, *458*, 190−193.

(3) Liu, X. H.; Zhang, L. Q.; Zhong, L.; Liu, Y.; Zheng, H.; Wang, J. W.; Cho, J.-H.; Dayeh, S. A.; Picraux, S. T.; Sullivan, J. P.; Mao, S. X.; Ye, Z. Z.; Huang, J. Y. *Nano Lett.* **2011**, *11*, 2251−2258.

(4) Morgan, D.; Van der Ven, A.; Ceder, G. *Electrochem. Solid-State Lett.* **2004**, *7*, A30−A32.

(5) Nishimura, S.-i.; Kobayashi, G.; Ohoyama, K.; Kanno, R.; Yashima, M.; Yamada, A. *Nat. Mater.* **2008**, *7*, 707−711.

(6) Yang, J.; Tse, J. S. *J. Phys. Chem. A* **2011**, *115*, 13045−13049.

(7) Dathar, G. K. P.; Sheppard, D.; Stevenson, K. J.; Henkelman, G. *Chem. Mater.* **2011**, *23*, 4032−4037.

(8) Lee, J.; Pennycook, S. J.; Pantelides, S. T. *Appl. Phys. Lett.* **2012**, *101*, 033901.

(9) Park, K.-S.; Xiao, P.; Kim, S.-Y.; Dylla, A.; Choi, Y.-M.; Henkelman, G.; Stevenson, K. J.; Goodenough, J. B. *Chem. Mater.* **2012**, *24*, 3212−3218.

(10) Islam, M. S.; Driscoll, D. J.; Fisher, C. A.; Slater, P. R. *Chem. Mater.* **2005**, *17*, 5085−5092.

(11) Molenda, J.; Ojczyk, W.; Świerczek, K.; Zajac, W.; Krok, F.; Dygas, J.; Liu, R.-S. *Solid State Ionics* **2006**, *177*, 2617−2624.

(12) Amin, R.; Maier, J.; Balaya, P.; Chen, D.; Lin, C. *Solid State Ionics* **2008**, *179*, 1683−1687.

(13) Amin, R.; Balaya, P.; Maier, J. *Electrochem. Solid-State Lett.* **2007**, *10*, A13−A16.

(14) Chung, S.-Y.; Bloking, J. T.; Chiang, Y.-M. *Nat. Mater.* **2002**, *1*, 123−128.

(15) Li, J.; Yao, W.; Martin, S.; Vaknin, D. *Solid State Ionics* **2008**, *179*, 2016−2019.

(16) Bennewitz, R.; Reichling, M.; Matthias, E. *Surf. Sci.* **1997**, *387*, 69−77.

(17) Shao, R.; Kalinin, S. V.; Bonnell, D. A. *Appl. Phys. Lett.* **2003**, *82*, 1869−1871.

(18) Balke, N.; Kalnaus, S.; Dudney, N. J.; Daniel, C.; Jesse, S.; Kalinin, S. V. *Nano Lett.* **2012**, *12*, 3399−3403.

(19) Yang, S.; Yan, B.; Li, T.; Zhu, J.; Lu, L.; Zeng, K. *Phys. Chem. Chem. Phys.* **2015**, *17*, 22235−22242.

(20) Schirmeisen, A.; Taskiran, A.; Fuchs, H.; Roling, B.; Murugavel, S.; Bracht, H.; Natrup, F. *Appl. Phys. Lett.* **2004**, *85*, 2053−2055.

(21) Ngai, K.; Wang, Y.-N.; Magalas, L. *J. Alloys Compd.* **1994**, *211*, 327−332.

(22) Funke, K. *Prog. Solid State Chem.* **1993**, *22*, 111−195.

(23) Ngai, K.; Kanert, O. *Solid State Ionics* **1992**, *53*, 936−946.

(24) Scher, H.; Shlesinger, M. F.; Bendler, J. T. *Phys. Today* **1991**, *44*, 26−34.

(25) Nowick, A.; Lim, B. *J. Non-Cryst. Solids* **1994**, *172*, 1389−1394.

(26) Jonscher, A. K. *J. Phys. D: Appl. Phys.* **1999**, *32*, R57.

(27) Schirmeisen, A.; Taskiran, A.; Bracht, H.; Roling, B. *Z. Phys. Chem. (Muenchen, Ger.)* **2010**, *224*, 1831−1852.

(28) Taskiran, A.; Schirmeisen, A.; Fuchs, H.; Bracht, H.; Roling, B. *Phys. Chem. Chem. Phys.* **2009**, *11*, 5499−5505.

(29) Schirmeisen, A.; Taskiran, A.; Fuchs, H.; Bracht, H.; Murugavel, S.; Roling, B. *Phys. Rev. Lett.* **2007**, *98*, 225901.

(30) Dokko, K.; Koizumi, S.; Nakano, H.; Kanamura, K. *J. Mater. Chem.* **2007**, *17*, 4803−4810.

(31) Nakamura, A.; Furutsuki, S.; Nishimura, S.-i.; Tohei, T.; Sato, Y.; Shibata, N.; Yamada, A.; Ikuhara, Y. *Chem. Mater.* **2014**, *26*, 6178−6184.

(32) Fisher, C. A.; Hart Prieto, V. M.; Islam, M. S. *Chem. Mater.* **2008**, *20*, 5907−5915.

(33) Paolella, A.; Bertoni, G.; Hovington, P.; Feng, Z.; Flacau, R.; Prato, M.; Colombo, M.; Marras, S.; Manna, L.; Turner, S.; Van Tendeloo, G.; Guerfi, A.; Demopoulos, G. P.; Zaghib, K. *Nano Energy* **2015**, *16*, 256−267.

(34) Cogswell, D. A.; Bazant, M. Z. *ACS Nano* **2012**, *6*, 2215−2225.

(35) Welland, M. J.; Karpeyev, D.; O'Connor, D. T.; Heinonen, O. *ACS Nano* **2015**, *9*, 9757−9771.

(36) Momma, K.; Izumi, F. *J. Appl. Crystallogr.* **2011**, *44*, 1272−1276.

(37) Prosini, P. P.; Lisi, M.; Zane, D.; Pasquali, M. *Solid State Ionics* **2002**, *148*, 45−51.

(38) Shi, S.; Liu, L.; Ouyang, C.; Wang, D.-s.; Wang, Z.; Chen, L.; Huang, X. *Phys. Rev. B: Condens. Matter Mater. Phys.* **2003**, *68*, 195108.

(39) Xu, Y.-N.; Chung, S.-Y.; Bloking, J. T.; Chiang, Y.-M.; Ching, W. *Electrochem. Solid-State Lett.* **2004**, *7*, A131−A134.

(40) Churikov, A.; Ivanishchev, A.; Ivanishcheva, I.; Sycheva, V.; Khasanova, N.; Antipov, E. *Electrochim. Acta* **2010**, *55*, 2939−2950.

DOI: 10.1021/acs.nanolett.7b01857
Nano Lett. 2017, 17, 4489−4496

(41) Liu, H.; Strobridge, F. C.; Borkiewicz, O. J.; Wiaderek, K. M.; Chapman, K. W.; Chupas, P. J.; Grey, C. P. *Science* **2014**, *344*, 1252817.
(42) Chapman, K. W. *MRS Bull.* **2016**, *41*, 231−240.

DOI: 10.1021/acs.nanolett.7b01857
Nano Lett. 2017, 17, 4489−4496